Applied Catalysis B: Environmental 341 (2024) 123350

Contents lists available at ScienceDirect

Applied Catalysis B: Environmental

journal homepage: www.elsevier.com/locate/apcatb

Enhanced contaminant degradation by FeS under oxic conditions with the coexistence of cobalt and nickel

Rongrong Ding [a], Guannan Zhou [a], Chuanshu He [a,b,*], Wenqiang Li [a], Yiran Wang [a], Xiaocheng Liu [a], Bo Lai [b], Yang Mu [a,**]

[a] CAS Key Laboratory of Urban Pollutant Conversion, Department of Environmental Science and Engineering, University of Science and Technology of China, Hefei, China

[b] Department of Environmental Science and Engineering, College of Architecture and Environment, Sichuan University, Chengdu 610065, China

ARTICLE INFO

Keywords:
FeS oxygenation
Fe(III)/Fe(II) circulation
Sulfur conversion
Heavy metals

ABSTRACT

The process of FeS oxygenation is intrinsically associated with the fate of contaminants in heterogeneous aquifers, whereas the impacts of common heavy metals are poorly understood. In this study, we found that the introduction of Co^{2+} and Ni^{2+} (Me^{2+}) resulted in a remarkable 3–10-fold enhancement in the degradation of bisphenol A, which stemmed from the significant increase in the generation of •OH and $SO_4^{\bullet-}$. The improved production of reactive species was primarily attributed to the accelerated regeneration of Fe(II); the introduction of Me^{2+} manipulated the electronic structure of FeS and consequently facilitated electron transfer from S^{2-} to Fe (III), as revealed by experimental evidence and density functional theory calculations. This study represents the first endeavor to underscore the influence of coexisting heavy metals on contaminant degradation during FeS oxygenation.

1. Introduction

FeS is formed through the bio-reduction of sulfate to sulfide, followed by successive reactions with iron oxide/hydroxide minerals, and is one of the most abundant natural iron sulfides [1,2]. This compound is widely distributed in reduced settings, including sediments of urban rivers, lakes, marine environments, and aquaculture ponds [3–5]. Nevertheless, various natural factors and human activities can collectively affect FeS-based redox conditions (i.e., anoxic or oxic atmosphere). For example, Kumar et al. investigated seasonal changes in dissolved oxygen (DO) within 65 shallow groundwater wells in the Chrompet area of Chennai city, India, showing that the shallow groundwater was oxic with DO levels spanning 0.25–5.00 mg/L [6]. Moreover, it is universal for contaminants to coexist with FeS within untreated or partially treated wastewater and sediments. Given its substantial specific surface area and reducibility, FeS inherently influences the migration and transformation of these coexisting contaminants. Notably, it has been reported that •OH can be generated by structural Fe(II) within FeS under oxic conditions, significantly contributing to the oxidation of contaminants, including metalloid As (III), and radionuclide U(IV) [7,8]. As such, the oxidation behavior of FeS is closely related to the fate of coexisting contaminants under both surface and subsurface environments.

On the other hand, a related issue is that an alarming increase in the use of heavy metals has led to an imminent explosion of heavy metals in aquatic environments [9,10]. Among these, cobalt (Co) and nickel (Ni) hold a distinct status as vital raw materials seldom substitutable by other elements, particularly in essential applications like lithium-ion batteries, jet engines, and petroleum refining. Large consumption inevitably results in the massive release of Co and Ni into the environment. It has been reported that in heavily polluted areas, such as the Upper Sakarya River Basin in Turkey, concentrations of Co and Ni in surface water can reach 5.3 and 10.2 ppm, respectively [11]. Areas near mining or leachate sites can even have metal ion concentrations in the range of several ppm to hundreds of ppm [12,13].

Heavy metals can be captured by FeS through adsorption, precipitation, or ion exchange with highly insoluble metal sulfides [14,15]. As a consequence, the physicochemical properties of FeS could in turn be

* Corresponding author at: CAS Key Laboratory of Urban Pollutant Conversion, Department of Environmental Science and Engineering, University of Science and Technology of China, Hefei, China.
** Corresponding author.
E-mail addresses: hecs@scu.edu.cn (C. He), yangmu@ustc.edu.cn (Y. Mu).

https://doi.org/10.1016/j.apcatb.2023.123350
Received 5 June 2023; Received in revised form 27 August 2023; Accepted 27 September 2023
Available online 29 September 2023

altered by the coexistence of heavy metals, thus affecting its ability to remove pollutants [16–18]. Previous studies have reported that CoS formed by the introduction of Co^{2+}, compared to original FeS, exhibited superior activity towards tetrachloroethylene dechlorination. However, in the Ni^{2+} coexistence system, dechlorination rates decreased due to the close association between the generated nickel sulfide and FeS, which hindered electron transfer from FeS to contaminants [19]. However, it was found that both Co^{2+} and Ni^{2+} boosted trichloroethylene reduction by Fe/FeS due to the formation of reactive hydrogen [20]. Collectively, the adsorption or co-precipitation of heavy metals on FeS could indeed affect the transformation of coexisting pollutants, and potentially affect the geochemical behavior of FeS.

Nonetheless, previous studies have predominantly concentrated on reactions occurring under anoxic conditions, while there remains no research investigating how heavy metals impact the oxidation of FeS for contaminant degradation. It has been reported that the oxidation of FeS was a surface-mediated process in which the surface Fe(II) converted oxygen into •OH, while only a small amount of S^{2-} was involved in the circulation of Fe(III)/Fe(II) with a negligible contribution to •OH production [7]. Recent studies have shown that $SO_4^{\bullet-}$ formation can be formed even in sulfidated β-FeOOH/H_2O_2 systems [21]. This is because sulfur species as an electron donor were oxidized by Fe(III) and H_2O_2 to form peroxymonosulfate and subsequently converted to $SO_4^{\bullet-}$. Moreover, the auto-oxidation of sulfite catalyzed by heavy metals in the presence of oxygen was crucial for the sulfur cycle and could generate the active intermediate $SO_4^{\bullet-}$ [22,23]. Considering that sulfite (SO_3^{2-}) is a key sulfur intermediate during FeS oxidation [24,25], the catalytic conversion of sulfur on the surface of FeS induced by heavy metals may play an important role in the formation of oxidative radicals during FeS oxygenation, which warrants further investigation.

In this study, the impacts of heavy metals on FeS oxygenation as well as the fate of aquifer contaminants were carefully investigated. Both Co^{2+} and Ni^{2+} (named Me^{2+}) were selected for this study since they are ubiquitous in the environment and potential coexistence with FeS. Bisphenol A (BPA), an endocrine disruptor with effects across various species [26,27], is widely found in plastics used for water bottles, food containers, and medical devices, rendering it a representative contaminant. Additionally, compounds like CIP, SMX, and 4-CP, which might coexist with BPA, were also included in the assessment. Scavenging experiments, electron paramagnetic resonance (EPR) analysis, and probe experiments were conducted to identify the reactive species involved in FeS and FeS/Me^{2+} systems. Moreover, electrochemical experiments and density functional theory (DFT) calculations were conducted to reveal the enhanced mechanism of reactive species generation during FeS oxygenation with the presence of Me^{2+}. Our study expands the current understanding of the influence of heavy metal ions on the geochemical behavior of FeS towards the transformation of aquifer contaminants under oxic conditions.

2. Materials and methods

2.1. Chemicals

FeS was synthesized according to the method reported by Butler and Hayes [3]. Specifically, a total of 72 mL of 0.55 M Na_2S was slowly added into 60 mL of 0.57 M $FeCl_2$ under stirring in the N_2-filled glove box. The resulting suspensions were aged for 3 days and then centrifuged at 11000 rpm for 8 min. The obtained solids were then re-dispersed in the deoxygenated water and centrifuged again about 5 times. Finally, the obtained FeS was used to prepare a stock solution and stored in the N_2-filled glove box. The synthesized particles were identified to be mackinawite (JCPDS: 86–0389) by X-ray diffraction (XRD) (Fig. S1). BPA, sulfamethoxazole (SMX), and ciprofloxacin (CIP) were purchased from Aladdin Chemistry (Shanghai, China). 5,5-dimethyl-1-pyrroline-*N*-oxide (DMPO) and 2,2,6,6-Tetramethylpiperidinooxy (TEMP) were obtained from Sigma-Aldrich Chemical Co., Ltd. (USA). *N*-(2-Hydroxyethyl) piperazine-*N*'-2-ethanesulfonic acid (HEPES) was purchased from Sangon Biotech Co., Ltd. (Shanghai, China). Methyl phenyl sulfoxide (PMSO) and methyl phenyl sulfone ($PMSO_2$) were bought from Energy Chemistry (Shanghai, China). Other chemicals, including tetrachlorophenol (4-CP), BA, salicylic acid (2-HBA), 3-hydroxybenzoic acid (3-HBA), 4-hydroxybenzoic acid (4-HBA), 2,5-dihydroxybenzoic acid (2,5-DHBA), phenol, $Na_2S{\cdot}9\ H_2O$, elemental sulfur, $Na_2S_2O_3$, Na_2SO_3, $FeCl_2{\cdot}4\ H_2O$, $CoCl_2{\cdot}6\ H_2O$, $NiCl_2{\cdot}4\ H_2O$, *tert*-butyl alcohol (TBA), benzoquinone (BQ) and ethyl alcohol (EtOH) were all purchased from Sinopharm Chemical Reagent Co., Ltd. (China). All chemicals were used as received without further purification. Deionized (DI) water was used in the preparations of all solutions unless otherwise noted. Real water was collected from a natural lake located at the University of Science and Technology of China (Anhui, China). The characteristics of real water are listed in Table S2.

2.2. Experimental procedures and analysis

All batch experiments were conducted in an open foil-covered conical flask (100 mL) under oxic conditions at 25 °C with magnetic stirring at 180 rpm. Typically, a precise volume of 0.5 M Me^{2+} stock solution (achieving a final concentration of 0.17–10 mM) is introduced into a 50 mL BPA solution (10 mg/L) or a HEPES-buffered solution (3 mM) containing 10 mM BA or 200 μM PMSO. All the solutions' pH values were adjusted to 7.00 ± 0.02 by adding hydrochloric acid or sodium hydroxide. The reaction was initiated by dosing a predetermined volume of FeS suspension stock. The choice of 1 g/L FeS aligns with standard sediment compositions and is supported by established literature [7,28–31]. In heavily polluted leachate-contaminated sites, concentrations of heavy metals can reach several tens of ppm, and BPA concentrations can exceed a dozen ppm [12,13,32–34]. Hence, we utilized a BPA range of 1–10 ppm in our study to simulate highly contaminated water environments affected by industrial wastewater or leachate. A Me^{2+} concentration of 10 mg/L was selected to evaluate its impact on the FeS oxidation process. Additionally, for a more in-depth exploration of underlying mechanisms, we deliberately employed higher Me^{2+} concentrations in subsequent investigations. The reaction time is related to the oxidation of Fe(II). We stop the reaction when Fe(II) is almost completely depleted. The solution without the addition of Me^{2+} was set as the control one. Reaction rate constants were calculated from the slope of the curve $\ln(C/C_0)$-t, where C and C_0 are BPA concentrations at sampling times. Scavenger experiments were conducted in the same reactor but with the addition of 2.0 mM BQ, 1.0 M TBA, and EtOH. The probe experiments were carried out in the reaction solution containing 10 mM BA with 3.0 mM HEPES buffer to quantify the generation of reactive oxidants, or the solution containing 200 μM PMSO to identify the presence of Fe(IV). Samples were periodically collected during the reaction and immediately analyzed. Most experiments were conducted with three replicates; error bars in the figures represent the standard deviation. However, certain tests, such as those involving time-consuming analysis of BA oxidation products, make it challenging to achieve three replicates. In such cases, we opted for two repetitions due to their excellent reproducibility.

Concentrations of BPA and the oxidation products of BA, BQ, PMSO, $PMSO_2$, and elemental sulfur were quantified with high-performance liquid chromatography (HPLC, 1260 Infinity, Agilent Inc., USA) with a diode array detector. When detecting low concentrations of BPA, the injection volume was changed from 20 μL to 100 μL. The insoluble elemental sulfur was extracted using *n*-hexane before HPLC analysis [35]. Targeted compounds were separated with an Agilent HC-C18 reversed-phase column (5 μm, 4.6 mm × 250 mm, 30 °C) at a flow rate of 1 mL/min. The detailed parameters for the analysis of the specific compounds are listed in Table S1.

BPA degradation intermediates were identified by a TripleTOF 5600 + high-resolution tandem mass spectrometry (LC-MS/MS, Applied Biosystems SCIEX, U.S.A.). Separation was accomplished with a Waters

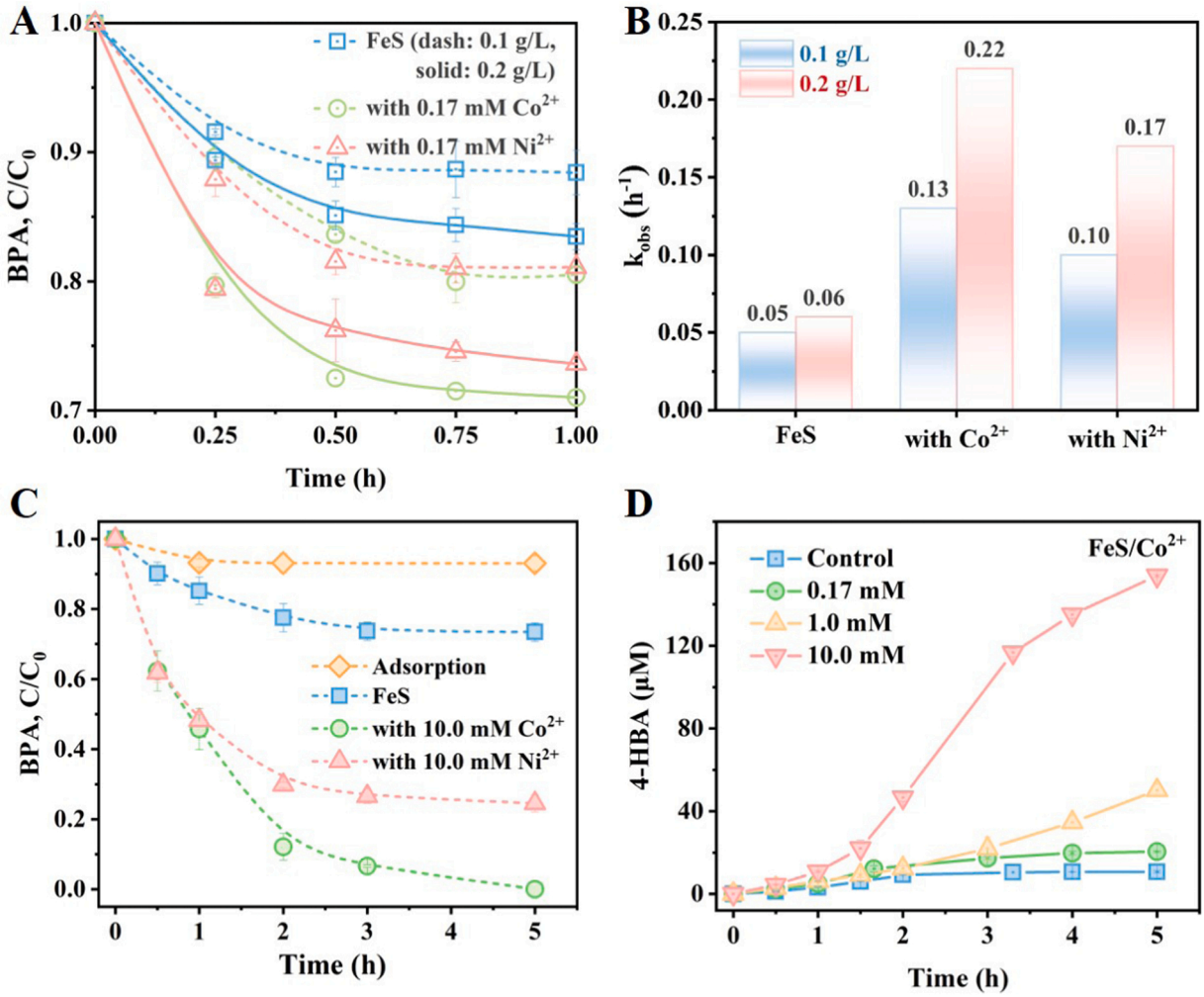

Fig. 1. (A) Influence of Co^{2+} and Ni^{2+} on the removal of BPA during the oxidation of FeS, (B) the corresponding pseudo-first-order kinetic analysis results, (C) effect of high concentration of Co^{2+} and Ni^{2+} on the removal of BPA during the oxidation of 1.0 g/L FeS, and (D) effect of Co^{2+} dosage on the generation of 4-HBA during the oxidation of 1.0 g/L FeS. Experimental conditions: 10.0 mg/L BPA (or 10.0 mM BA for trapping •OH), pH 7.0, unless otherwise specified.

Symmetry C-18 column (2.1 × 150 mm, 3.5 μm) at 40 °C, and gradient method was methanol/water at a flow rate of 0.3 mL/min with a ratio as follows: 0–5.0 min, 20/80 (v/v); 5.0–12 min, 55/45 (v/v); 12.0–15.0 min, 80/20 (v/v); 15.0–18.0 min, 20/80 (v/v). The electrospray ionization needle voltage was set at 3.0 kV in negative ionization mode for MS/MS fragmentation with *m/z* 40–600.

Dissolved oxygen (DO) concentrations were monitored during the oxidation process using the LDO™ portable Oxygen dissolving instrument (HQ30D, HACH, USA). Dissolved Fe(II) and total Fe(II) (dissolved by 6.0 M HCl) were determined by a 1,10-phenanthroline colorimetric method at 510 nm [36]. Under buffered conditions at pH 7.0, the concentration of Fe(III) in the system is almost negligible. Therefore, we can readily calculate the concentration of solid phase Fe(III) using the equation: Solid Fe(III) = Total Fe - Total Fe(II). The morphology of the FeS particles was characterized with a field emission transmission electron microscope (TEM) (JEM 2100 F, JEOL Ltd., Japan). X-ray diffraction (XRD) patterns were observed with a Japan Rigaku Smatlab X-ray diffractometer using Cu Kα (λ = 0.154056 nm) irradiation. Valence states of elements were obtained by X-ray photoelectron spectroscopy (XPS, ESCALAB 250, Thermo-VG Scientific S). Functional groups of fresh FeS and the solid products in the FeS and FeS/Me^{2+} systems under oxic conditions were analyzed by Fourier transform infrared spectroscopy (FTIR, Nicolet 6700, Thermo Fisher, USA) and diffuse reflectance FTIR (DRFTIR) (TENSOR II Sample Compartment RT-DLaTGS). Electron paramagnetic resonance (EPR, JES-FA200, JEOL Ltd., Japan) was applied to identify the reactive species using DMPO and TEMP as spin-trapping agents. Soluble sulfur was detected using an inductively coupled plasma atomic emission spectrometer (ICP-AES, Optima 7300 DV, PerkinElmer, USA). The supernatant was collected and freeze-dried to analyze the oxidation products of sulfur using Time-of-flight secondary-ion mass spectrometry (TOF-SIMS) (TOF-SIMS 5–100, ION-TOF GmbH, Germany). Raman analysis was carried out using a confocal microscopic Raman spectrometer (LabRam HR, Horiba, France) with a 1024-pixel LN/CCD detector using the 532 nm emission line. Tafel analysis was conducted on a potentiostat (VMP3, Bio-Logic Science Instruments, France) in a standard three-electrode system with 10 mM NaCl as electrolyte. Working electrodes were prepared by depositing the sample onto a fluorine-doped tin oxide (FTO) glass surface.

2.3. DFT calculations

DFT calculations were carried out to evaluate changes in the electronic structure of FeS after the introduction of Me^{2+}. All calculations were performed according to the first-principles DFT using the Cambridge Serial Total Energy Package (CASTEP) [37]. The electron exchanges and correlation energies were described by generalized gradient approximation (GGA) with a Perdew-Burke-Ernzerhof (PBE) functional [38]. The cut-off energy, convergence criteria for maximum energy, and force convergence were set to 390.0 eV, 5 × 10^{-6} eV/atom,

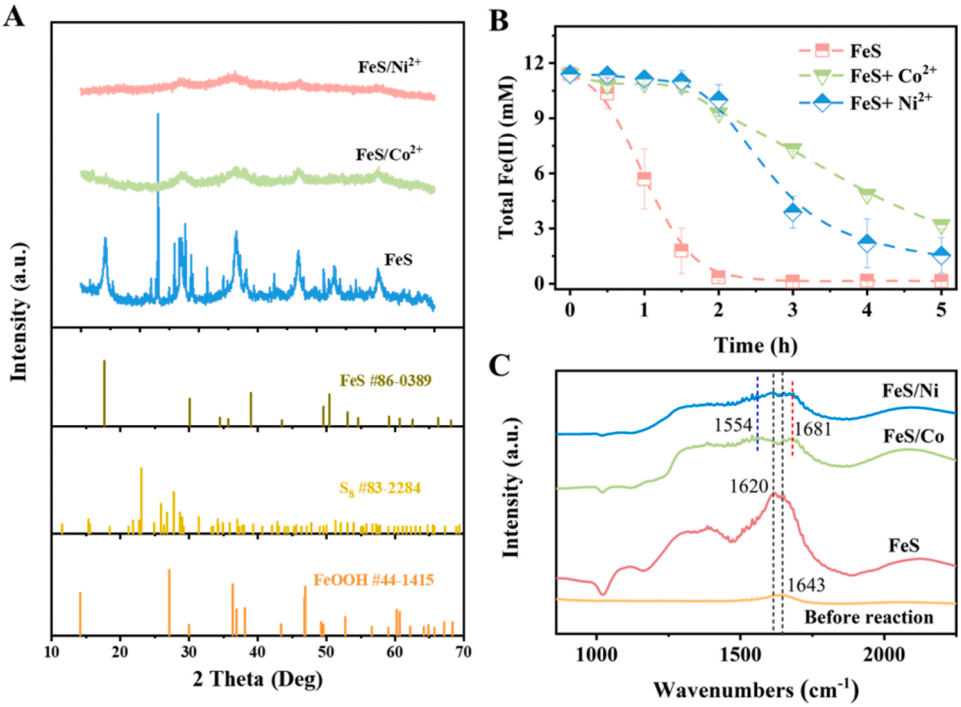

Fig. 2. (A) XRD patterns of the oxidation products after 5 h reaction in FeS and FeS/Me^{2+} systems under oxic conditions, (B) Concentration variations of the total Fe (II), and (C) DRFTIR of Fresh FeS and the solid products after 1 h reaction. Experimental conditions: 1.0 g/L FeS, 10.0 mM Me^{2+}, pH 7.0.

and 0.01 eV/Å, respectively. FeS(001) - p(3 × 1) supercells were modeled with a vacuum layer of 15 Å. Me-Fe ion exchange generally occurred in the FeS and Me^{2+} coexistence systems. Hence, the FeS/Co (001) and FeS/Ni(001) models were constructed by replacing one of the top Fe atoms with a Co or Ni atom. The k-points for bulk FeS and surface calculations were determined to be 7 × 7 × 5 and 2 × 6 × 1 by the Monkhorst-Pack algorithm [39], respectively.

3. Results and discussion

3.1. BPA degradation and FeS transformation under oxic conditions

To understand the impact of Me^{2+} on BPA degradation with FeS under oxic conditions, oxidation experiments involving FeS coexisting with 0.17 mM Co^{2+} or Ni^{2+} were conducted. As shown in Fig. 1A and 1B, 0.17 mM Co^{2+} or Ni^{2+} resulted in approximately 4- and 3-fold improvements in the degradation of BPA, respectively, at the specified experimental conditions (0.2 g/L FeS). Moreover, BPA degradation was further improved with the increase of FeS amount and Me^{2+} dosage. Approximately 76% of BPA was eliminated from the FeS/Ni^{2+} system and 100% from the FeS/Co^{2+} system after a 5-hour reaction, compared to only 27% degradation in the FeS system (Fig. 1C). BPA degradation followed pseudo-first-order kinetics, yielding reaction constants of 0.10, 1.06, and 0.53 h^{-1} for FeS, FeS/Co^{2+}, and FeS/Ni^{2+}, respectively (Fig. S2). To assess the oxidation behavior in real water relevant to the application, kinetic experiments were conducted in a real water matrix with a low BPA concentration (1.0 mg/L). As shown in Fig. S3, even with a real-world water matrix, the removal of low-level BPA was also expedited in FeS/Me^{2+} systems compared to FeS ones. As such, the presence of Me^{2+} notably boosted BPA degradation in the FeS system, with FeS/Co^{2+} exhibiting the strongest enhancement. We also conducted additional experiments to degrade a mixture consisting of SMX, CIP and 4-CP, which is of interest due to the prevalent occurrence in leachate-contaminated aquifers. Our results demonstrate that even in mixed systems with multiple pollutants, the presence of Me^{2+} remains effective in enhancing contaminants degradation during FeS oxygenation (Fig. S4). For the sake of more clearly exploring its internal mechanism, a high concentration of Me^{2+} was selected for subsequent exploration.

We noticed that the initially black FeS suspension gradually turned into yellow precipitates within 2 h when Me^{2+} was absent. Interestingly, in the presence of Me^{2+}, the suspension consistently retained its black appearance (Fig. S5). This observation hints at the potential influence of Me^{2+} on altering the oxidation dynamics of FeS under oxic conditions. Subsequently, we employed XRD to examine the phase transformation of FeS after 5 h (Fig. 2A). Remarkably, in the absence of Me^{2+}, notable signals corresponding to FeOOH (lepidocrocite) and S_8 (elemental sulfur) emerged. However, when Me^{2+} was introduced, only a weak lepidocrocite signal was observed. Generally, faster degradation of BPA requires the formation of more reactive oxidants in the system, which means that the more electrons given by the FeS are required for O_2 activation, the faster FeS is consumed. However, the decline of total Fe (II) is more significant in the FeS system compared to the FeS/Me^{2+} systems (Fig. 2B). Moreover, in the FeS/Ni^{2+} system, the characteristic FeS peaks consistently persist in XRD patterns during the initial 2-hour reaction period, while these peaks are absent in the FeS system, implying the fast consumption of FeS (Figs. S6). Both XRD analysis and Fe(II) variation corroborate the observation that the presence of Me^{2+} decelerates the oxidation of FeS.

The turnover frequency (TOF) was determined by using Eqs. 1 and 2.

$$\mathrm{TOF} = \frac{\bullet\mathrm{OH\ accumulation}}{\mathrm{Fe(II)\ consumption} * \mathrm{reaction\ time}} \quad (1)$$

$$\bullet\mathrm{OH\ accumulation} = C_{2\text{–HBA}} + C_{3\text{–HBA}} + C_{4\text{–HBA}} + C_{2,5\text{–DHBA}} \times 2 \quad (2)$$

where $C_{2\text{-HBA}}$, $C_{3\text{-HBA}}$, $C_{4\text{-HBA}}$ and $C_{2,5\text{-DHBA}}$ are the concentrations of 2-HBA, 3-HBA, 4-HBA and 2,5-DHBA, respectively.

The calculated TOF value was 0.002, 0.050, and 0.016 h^{-1} for FeS, FeS/Co^{2+} and FeS/Ni^{2+} systems, respectively, clearly suggesting that the oxidative degradation of BPA during FeS oxygenation was significantly boosted in the presence of Me^{2+}. Under similar experimental

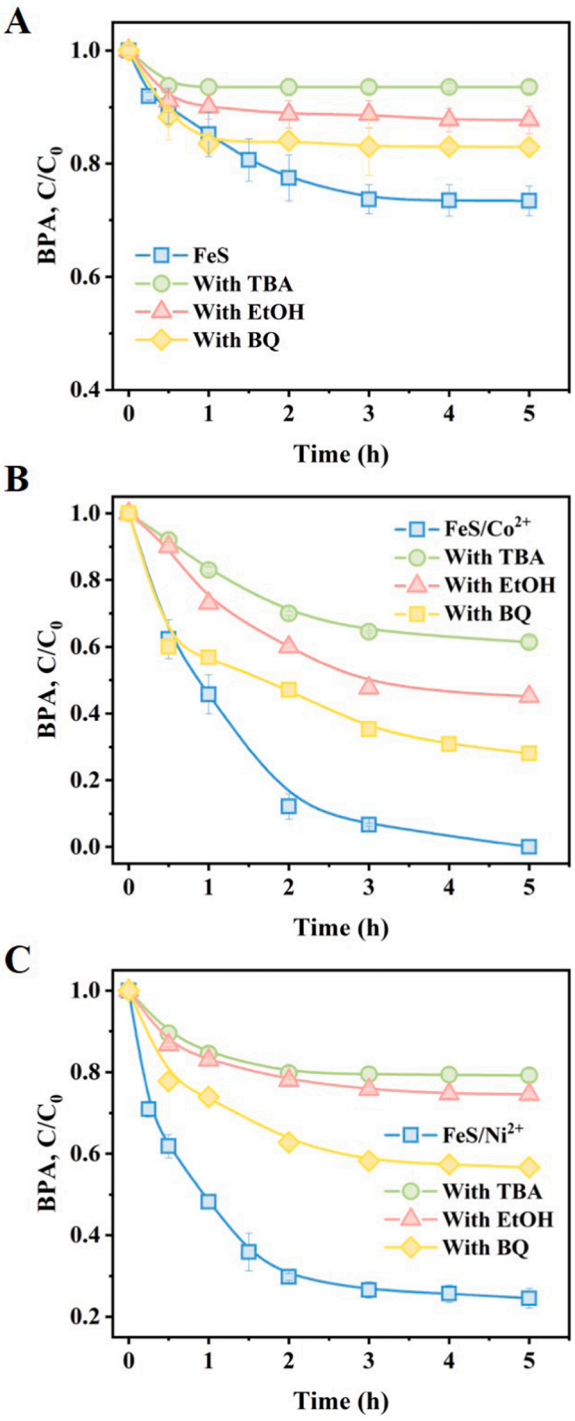

Fig. 3. Effects of radical scavengers on BPA degradation (A) FeS system, (B) FeS/Co^{2+} system, and (C) FeS/Ni^{2+} system under oxic conditions. Experimental conditions: 10.0 mg/L BPA, 1.0 g/L FeS, Me^{2+} 10.0 mM, 1.0 M TBA, 1.0 M EtOH, 2.0 mM BQ, pH 7.0.

conditions, our study observed degradation rate constants for pollutants within the range of 0.1–0.53 h^{-1}, which is comparable to the reported 0.13 h^{-1} by Cheng et al. using FeS and 0.10 h^{-1} by Liu et al. using Fe@Fe_2O_3 core–shell nanowires [8,40].

3.2. Identification of involved reactive species

It was established that the dissolved Fe(II) concentration in the FeS/Me^{2+} system was notably low (Fig. S7), which would unlikely result in a significant homogeneous oxidation for BPA degradation. Moreover, the introduction of an additional 10 mM Fe^{2+} exhibited limited enhancement in BPA degradation in the FeS/Me^{2+} system (Fig. S8). We also observed that fewer reactive oxidants were generated in the systems containing Me^{2+} and different sulfur species (S^0, $S_2O_3^{2-}$ and SO_3^{2-}) but lacking Fe(II) (Table S3). In addition, it has been reported that the oxidation of FeS was a surface-mediated process, involving the activation of O_2 by structural Fe(II) on the FeS surface for the generation of •OH [7]. All of the above results suggested that the surface-mediated oxidation process would be dominant to the BPA degradation in the FeS/Me^{2+} system.

Table 1
The distribution of different BA oxidation products generated in FeS and FeS/Me^{2+} systems under oxic conditions at the reaction time of 5 h. Experimental conditions: 1.0 g/L FeS, 10.0 mM BA, 10.0 mM Me^{2+}, pH 7.0.

	Percentage of products (%)				
	2-HBA	3-HBA	4-HBA	2,5-DHBA	Phenol
FeS	9	23	22	46	0
FeS/Co^{2+}	19	23	26	28	4
FeS/Ni^{2+}	17	31	27	18	7

Scavenger experiments were performed to identify the primary reactive oxidants responsible for BPA degradation. Specifically, 2.0 mM BQ, 1.0 M TBA, and EtOH were used to quench $O_2^{\bullet-}$, •OH, and $SO_4^{\bullet-}$/•OH, respectively. Apart from the adsorption of BPA by FeS, the introduction of TBA in the FeS system significantly suppressed BPA removal (Fig. 3A), underscoring the prominent role of •OH in BPA degradation. However, in FeS/Me^{2+} systems, BPA degradation was only partially hindered by TBA addition (Fig. 3B and C), suggesting the involvement of other reactive species besides •OH. Notably, the inhibitory effect of EtOH was milder compared to TBA, indicating that BPA predominantly experiences heterogeneous degradation on the FeS surface. This is attributed to the higher surface affinity of TBA toward FeS due to its lower dielectric constant than EtOH [41], leading to greater adsorbed •OH quenching by TBA. Additionally, the BPA degradation efficiencies also decreased after adding BQ, suggesting the participation of $O_2^{\bullet-}$ in both FeS and FeS/Me^{2+} systems. This can be attributed to the fact that the activation of O_2 by FeS was a continuous one-electron process and $O_2^{\bullet-}$ acts as the important intermediate for the final formation of •OH (Eqs. 3–5).

$$O_2 + H^+ + Fe(II) \rightarrow HO_2^{\bullet} + Fe(III) \quad (3)$$

$$HO_2^{\bullet} + H^+ + Fe(II) \rightarrow H_2O_2 + Fe(III) \quad (4)$$

$$H_2O_2 + Fe(II) \rightarrow OH^- + {\bullet}OH + Fe(III) \quad (5)$$

To delve further into the identification of the reactive oxidants involved in the FeS oxidation process, BA was selected as the probe molecule due to its tendency to produce hydroxylation products and phenol as primary outcomes upon reacting with •OH and $SO_4^{\bullet-}$, respectively [42,43]. It should be noted that the measured concentrations of the various oxidation products of BA could be regarded as those formed, considering that their adsorption onto the oxidation products of FeS remains relatively limited (5.2–7.5%) (Table S4). As depicted in Fig. 1D, S9, and S10, the concentrations of distinct oxidation products of BA exhibited notable increments with escalating Me^{2+} dosages. The concentrations of the oxidation products of BA at 5 h are listed in Table 1. Notably, no phenol was generated during FeS oxygenation, in line with prior findings [44]. However, it is worth noting that phenol was generated when Me^{2+} coexisted with FeS, indicating the existence of $SO_4^{\bullet-}$. The relatively low proportion of phenol produced in FeS/Me^{2+} systems (Table 1) indicated that $SO_4^{\bullet-}$ made only a limited contribution to BPA degradation compared to the predominant •OH production in FeS/Me^{2+} systems.

Furthermore, we employed electron paramagnetic resonance (EPR)

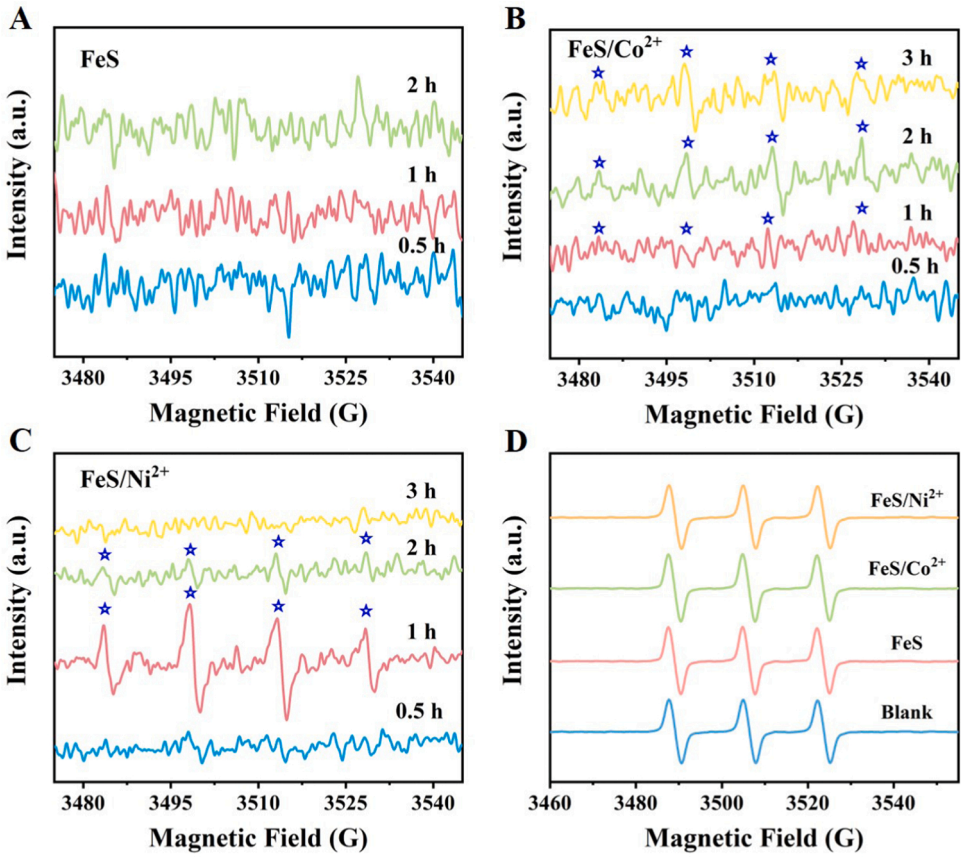

Fig. 4. EPR spectra of •OH generated in (A) FeS system, (B) FeS/Co^{2+} system, and (C) FeS/Ni^{2+} system at different reaction times, and (D) EPR spectra of $^1O_2$ in FeS and FeS/Me^{2+} systems under oxic conditions at the reaction time of 1 h. Experimental conditions: 1.0 g/L FeS, 10.0 mM Me^{2+}, pH 7.0.

analysis to delve into the reactive species involved (Fig. 4). The signals of DMPO•-OH intensified after the addition of Me^{2+} (Fig. 4B and C), indicating that Me^{2+} significantly expedited •OH generation. No distinct DMPO•-OH signal was observed in the FeS system (Fig. 4A), indicating the low concentration of •OH. However, the $SO_4^{\bullet-}$ signal in the EPR spectra is notably faint, attributed not only to its low concentration but also to the inherent weak response of $SO_4^{\bullet-}$ [45]. Alternatively, we adopted in-situ Raman experiments to ascertain the formation of $SO_4^{\bullet-}$ in FeS/Me^{2+} systems. As anticipated, the detection of HSO_5^-, an intermediate in the generation of $SO_4^{\bullet-}$, in FeS/Me^{2+} systems substantiated the presence of $SO_4^{\bullet-}$ (Fig. S11). Furthermore, the formation of benzoquinone (BQ) (Fig. S12), the main by-product of the reaction between $SO_4^{\bullet-}$ and 4-HBA (one BQ formation consumes one $SO_4^{\bullet-}$), provided additional validation for the production of $SO_4^{\bullet-}$ in FeS/Me^{2+} systems [46]. Moreover, the signal of TEMP-$^1O_2$ remained unchanged in the FeS system, irrespective of the presence of Me^{2+}, underscoring the negligible involvement of $^1O_2$ in BPA degradation (Fig. 4D). Since Fe(IV) can form in a neutral pH environment via the Fenton reaction, PMSO was selected as the probe compound for specific identification [47,48]. The extremely low conversion efficiency (< 1.5%) of PMSO to $PMSO_2$ (Fig. S13) indicated that Fe(IV) did not constitute a primary oxidant generated during FeS oxygenation. Taking into account the findings discussed above, we can conclude that the introduction of Me^{2+} not only remarkably enhanced the generation of •OH, but also facilitated the production of $SO_4^{\bullet-}$. Furthermore, the concentrations of •OH and $SO_4^{\bullet-}$ were quantified. The precise concentrations are detailed in Table S5, showcasing a considerable increase in •OH in the Me^{2+} coexisting system by an order of magnitude.

To clarify the BPA oxidation mechanism, the oxidative degradation intermediates of BPA in both FeS and FeS/Me^{2+} systems were detected by LC-MS/MS. The details of the intermediates are listed in Table S6 and consequently the possible pathways of BPA oxidation are suggested in Figs. S14 and S15. With the oxidization of BPA by •OH, monohydroxylated o-substituted BPA molecule (*m/z*: 243) and the corresponding quinone form (*m/z*: 241) were detected in the FeS system (Fig. S13). Moreover, 4-(2-hydroxypropan-2-yl) phenol (*m/z*: 152) and phenol molecules (*m/z*: 94) were also found in this system, which was formed through the β-scission of BPA by •OH. It should be noted that no ring-opening products were detected, but the polymerization products of BPA (*m/z*: 454) were detected. These results indicated that the mineralization of BPA during FeS oxygenation was limited with the absence of Me^{2+}. In the FeS/Me^{2+} system, the oxidative degradation of BPA was significantly intensified, where more intermediates, including ring-opening products, were detected (Fig. S15). Unlike the FeS system in the absence of Me^{2+}, the generated aromatic intermediates were further attacked by •OH and $SO_4^{\bullet-}$, leading to the generation of acetone (*m/z*: 58) via ring open reactions, and finally completely mineralized to CO_2 and H_2O. In light of existing literature, it has been determined that the acute and developmental toxicities of the BPA intermediates (i.e., phenol) investigated in this study are notably lower than those of BPA [49,50].

3.3. *Accelerated Fe(III)/Fe(II) circulation coupled with high-valence sulfur formation*

To understand whether pH changes predominantly influence the differential effect of Me^{2+} on FeS oxidation behavior, we compared the pH of FeS, FeS/Me^{2+}, and FeS/Fe^{2+} systems after 5 h of reaction, with an initial pH of 7.0 and no buffering salts added (Fig. S16). We observed pH values of 5.41, 3.99, 4.17, and 3.60 for the FeS, FeS/Co^{2+}, FeS/Ni^{2+}, and FeS/Fe^{2+} systems, respectively. The primary reason for the pH decrease in both the FeS and FeS/Fe^{2+} systems is the hydrolysis of Fe(III)

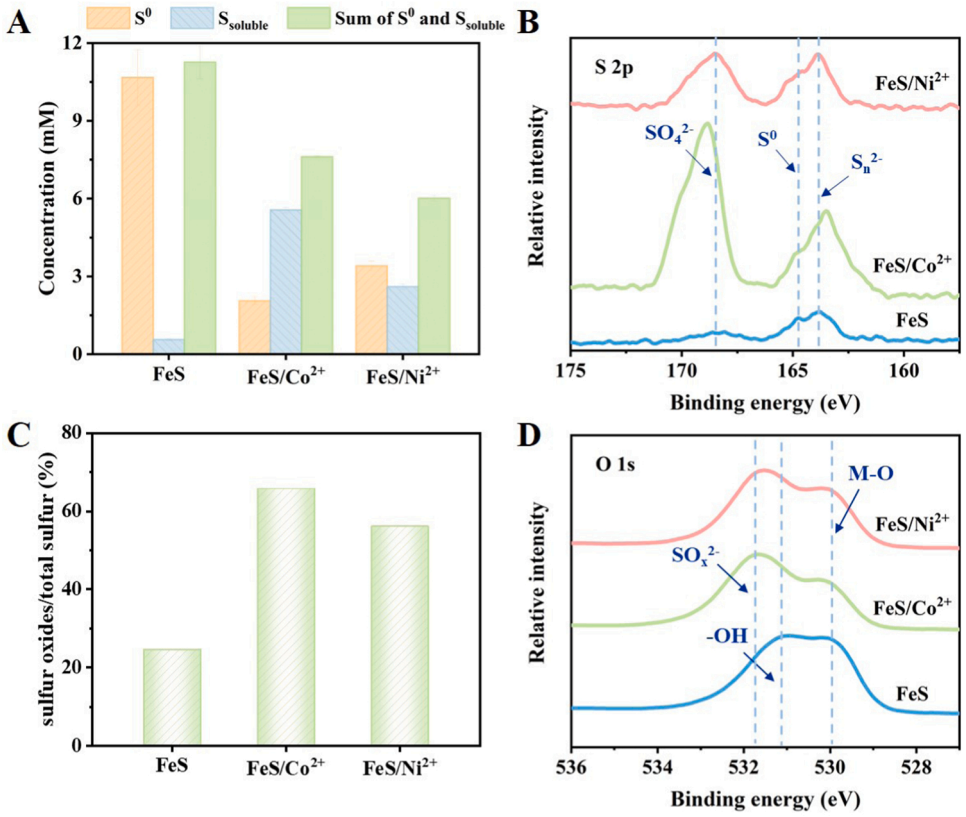

Fig. 5. (A) Production of elemental sulfur and dissolved sulfur, (B) XPS spectra of S 2p, (C) ratio of oxidized sulfur to total sulfur based on XPS analysis, and (D) XPS spectra of O 1 s of the oxidation products after 5 h in FeS and FeS/Me^{2+} systems under oxic conditions. Experimental conditions: 1.0 g/L FeS, 10.0 mM Me^{2+}, pH 7.0.

with the release of protons. The pH decrease in the FeS/Co^{2+} and FeS/Ni^{2+} systems is also linked to the oxidation of S^{2-}, resulting in the formation of sulfur oxides in these systems (Eq. 8). Notably, despite the FeS/Fe^{2+} system showing the most significant pH drop, its impact on BPA degradation enhancement remains limited (Figs. S16 and S8). Moreover, under the HEPES buffer solution, the addition of Me^{2+} significantly promoted the generation of reactive oxidants with negligible changes in pH (Figs. S10 and S17). The above results collectively demonstrate that the pH decrease induced by Me^{2+} addition is not the primary reason for promoted BPA degradation in FeS/Me^{2+} systems.

Notably, the formation of BA oxidation products was highly correlated with the total concentrations of Fe(II) (Fig. 2B and S18). Moreover, in the absence of Fe(II), no reactive oxidant was generated in the systems containing Me^{2+} and different sulfur species (S^0, $S_2O_3^{2-}$, and SO_3^{2-}) (Table S3). These findings strongly indicate that •OH generation in the FeS system primarily arises from the oxidation of Fe(II), regardless of the presence or absence of Me^{2+}. The higher concentration of dissolved Fe (II) after 2 h under pH 7.0 in the FeS/Me^{2+} system compared to the FeS one (Fig. S7) implied that Fe(II) was rapidly regenerated in the FeS/Me^{2+} system, otherwise, the dissolved Fe(II) at neutral pH will be rapidly depleted by oxidation. Moreover, the FeS/Me^{2+} systems exhibited a considerably shallower slop of the correlation between total Fe(II) and accumulated •OH compared to the FeS system (Fig. S19), thereby providing further support for the occurrence of a rapid Fe(II) regeneration process in the presence of Me^{2+}, consequently promoting the generation of •OH. The faster Fe(III)/Fe(II) circulation in the FeS/Co^{2+} system ensured a sustained and effective generation of •OH even after 1 h of reaction.

Furthermore, we conducted Raman analysis of the particles from both the FeS and FeS/Me^{2+} systems after the reaction time of 5 h to further understand the mineral composition. We find that the particles in the FeS system predominantly consist of lepidocrocite and elemental sulfur (S_8), while the oxidation products in FeS/Me^{2+} systems are primarily goethite, along with the presence of lepidocrocite and S_8 (Fig. S20). It has been reported that the persistent attachment and oxidation of Fe(II) on the lepidocrocite surface contributes to the formation of goethite [51]. Thus, it is concluded that in systems where Me^{2+} coexist, Fe(II) regeneration was promoted, and the continuous oxidation of the regenerated Fe(II) enables the transformation of lepidocrocite to goethite. Since the total Fe(III) concentrations for the FeS, FeS/Co^{2+}, and FeS/Ni^{2+} systems after 5 h of reaction were found to be 11.34, 8.40, and 9.88 mM, respectively (Fig. S21), the weak lepidocrocite signals in XRD spectra of the FeS/Me^{2+} systems were likely due to the rapid regeneration and re-oxidation of Fe(II) on the surface of FeS particles (Fig. 2A), thereby promoting the generation of •OH.

Typically, S^{2-} within FeS undergoes oxidization to elemental sulfur in oxic systems (Eq. 6). However, only a small amount of S^{2-} participates in the circulation of Fe(III)/Fe(II) (Eq. 7) [25], as supported by the similarity in 2, 5-DHBA (the main oxidative product of BA) yield between the Fe^{2+} and FeS systems (Fig. S18). Intriguingly, most of the sulfur species were oxidized to dissolved sulfur rather than elemental sulfur in the presence of Me^{2+} (Fig. 5A). Moreover, the dissolved sulfur in the FeS/Co^{2+} system was characterized by TOF-SIMS, in which $S_2O_3^-$, SO_3^-, HSO_3^-, SO_4^-, and HSO_4^- were detected, with SO_3^- as the predominant component (Fig. 6). Complementary XPS analysis (Fig. 5B-5D) indicated elevated sulfur oxide formation in FeS/Me^{2+} systems compared to FeS systems, suggesting Me^{2+} facilitated the transformation of sulfur into higher-valence sulfur oxides. Moreover, it has been mentioned in several literature that S^{2-} contributes to Fe(III) reduction [21,50]. In our study, the introduction of Me^{2+} accelerates the redox reaction of sulfur, which is evidenced by the increased corrosion current (icorr), the decreased polarization resistance (Rp) (Fig. 7 and Table S7), and the prevalence of SO_3^{2-} as the main oxidized sulfur component in the FeS/Co^{2+} system (Fig. 6). Finally, it is concluded that $SO_4^{\bullet-}$ was formed from SO_3^{2-}, the

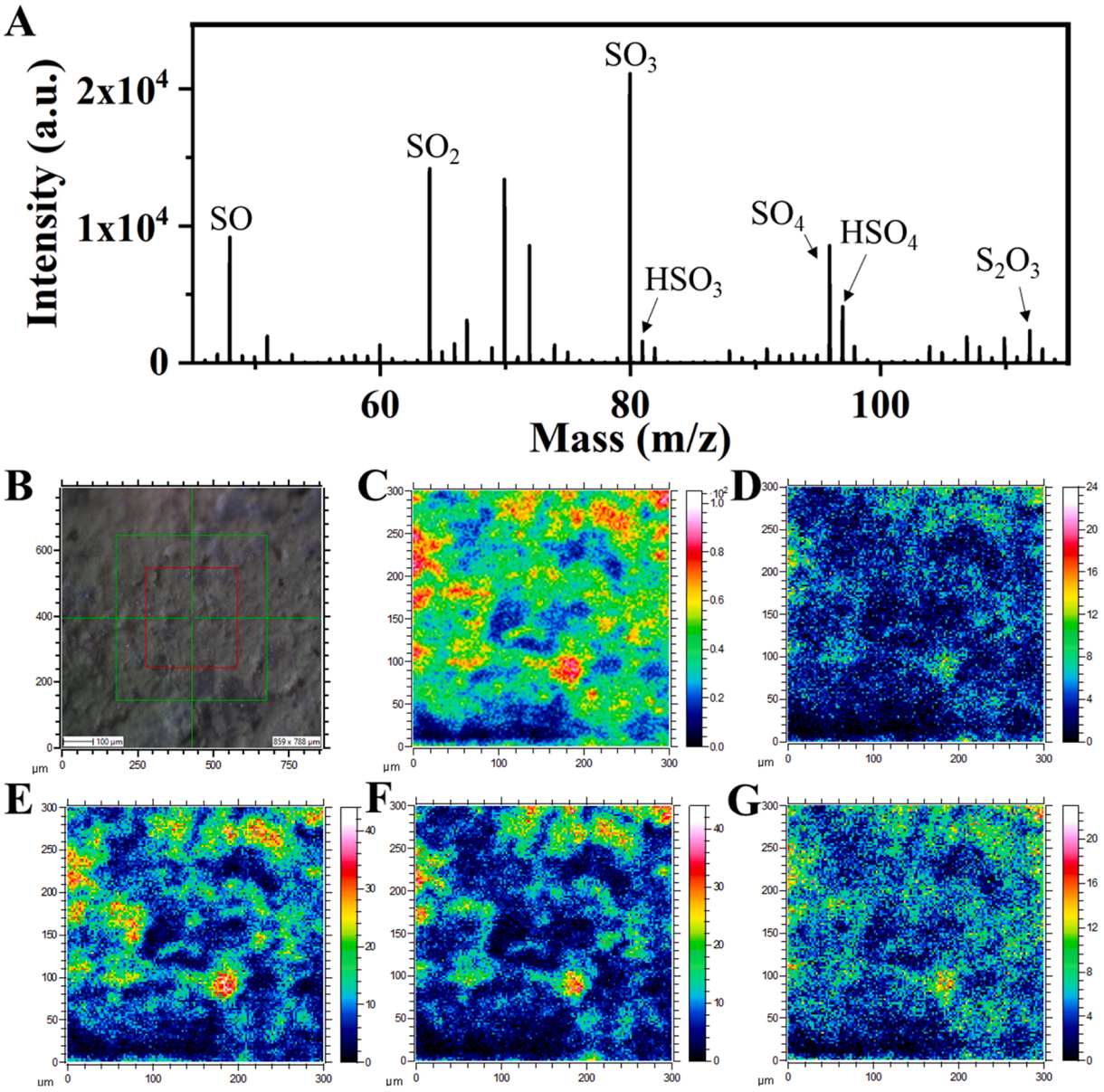

Fig. 6. (A) TOF-SIMS spectra, TOF-SIMS maps of (B) analyzed area, (C) SO_3^-, (D) HSO_3^-, (E) SO_4^-, (F) HSO_4^-, (G) $S_2O_3^-$ collected from the powder of the freeze-dried supernatant in FeS/Co^{2+} system after 5 h.

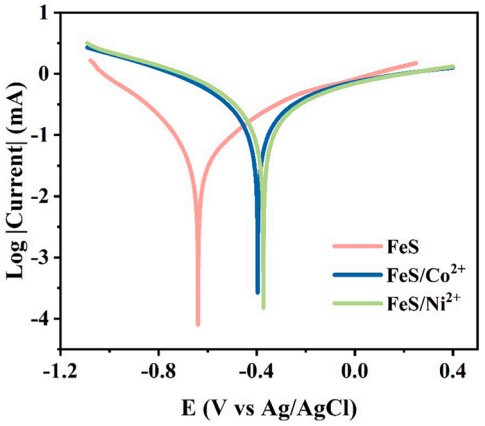

Fig. 7. Tafel analysis of working electrode made from FeS and aged FeS in Me^{2+} solutions.

oxidation product of S^{2-} catalyzed by Me^{2+} (Eq. 8) [22,52].

Moreover, we monitored the variation of DO concentration during the FeS oxygenation process (Fig. S22). It was observed that the DO concentration was maintained at a low level of less than 2.0 mg/L for the first-hour reaction, regardless of the absence or presence of Co^{2+} or Ni^{2+}, while increased to 8.0 mg/L in FeS system and around 4.0 mg/L in FeS/Me^{2+} systems after 3 h reaction, respectively. Significantly, the observation of slower Fe(II) oxidation coupled with faster-dissolved oxygen (DO) consumption in the FeS/Me^{2+} system, in comparison to the FeS system (Fig. 2B and S22), suggests the existence of alternative O_2 consumption pathways within the FeS/Me^{2+} environment for the enhancement of reactive oxidants generation. This phenomenon is due to the conceivable catalytic oxidation of S^{2-} by Me^{2+} with the consumption of O_2 to form high-valence sulfur oxides [22,53], as evidenced by the higher concentrations of high-valence dissolved sulfur species in the FeS/Me^{2+} systems.

$$2H^+ + O_2 + 2S^{2-} \rightarrow 2S^0 + 2OH^- \quad (6)$$

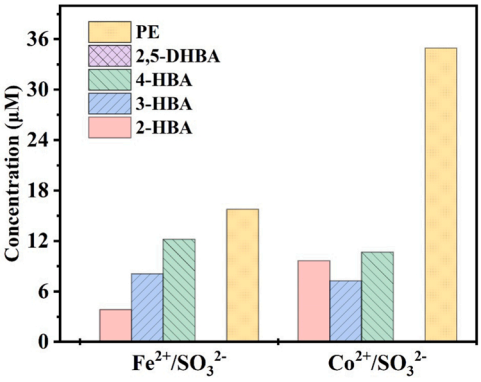

Fig. 8. Oxidation of BA in Fe^{2+}/SO_3^{2-} and Co^{2+}/SO_3^{2-} systems after 5 h under oxic conditions. Experimental conditions: 10.0 mM BA, 10 mM sulfite, the concentration of metal ions was 10.0 mM, pH 7.0.

$$2Fe(III) + S^{2-} \rightarrow S^0 + 2Fe(II) \quad (7)$$

$$H_2O + S^{2-} + Fe(III) \longrightarrow^{Me^{2+}} \text{intermediates} \longrightarrow^{Me^{2+}} SO_3^{2-} + Fe(II) + H^+ \quad (8)$$

On the other hand, since S^0, $S_2O_3^{2-}$, and SO_3^{2-} were formed in FeS/Me^{2+} systems (Fig. 6), a series of experiments with different sulfur intermediates were carried out to ascertain the sulfur species responsible for the generation of $SO_4^{\bullet-}$. We found that $SO_4^{\bullet-}$ was identified as the main oxidant generated in the Fe^{2+}/SO_3^{2-} and Co^{2+}/SO_3^{2-} systems. This conclusion was supported by the dominance of phenol as the product, with the absence of 2,5-DHBA formation (Fig. 8), but no phenol was generated in Me^{2+}/S^0, $Me^{2+}/S_2O_3^{2-}$ and Ni^{2+}/SO_3^{2-} systems (Table S3). As revealed that SO_3^{2-} was the main component of dissolved sulfur species in the FeS/Co^{2+} system (Fig. 6), which has been demonstrated to be catalyzed by transition metals to generate $SO_4^{\bullet-}$ (Eqs. 9–11) [22,52]. Therefore, the generation of $SO_4^{\bullet-}$ in FeS/Me^{2+} systems should originate from reactions between the formed SO_3^{2-} and Fe^{2+} or Co^{2+}. The absence of $SO_4^{\bullet-}$ formation in the FeS system can be attributed to the comparatively lower generation of SO_3^{2-} from S^{2-} in FeS (Fig. 5).

$$SO_3^{2-} + Fe(III) \rightarrow SO_3^{\bullet-} + Fe(II) \quad (9)$$

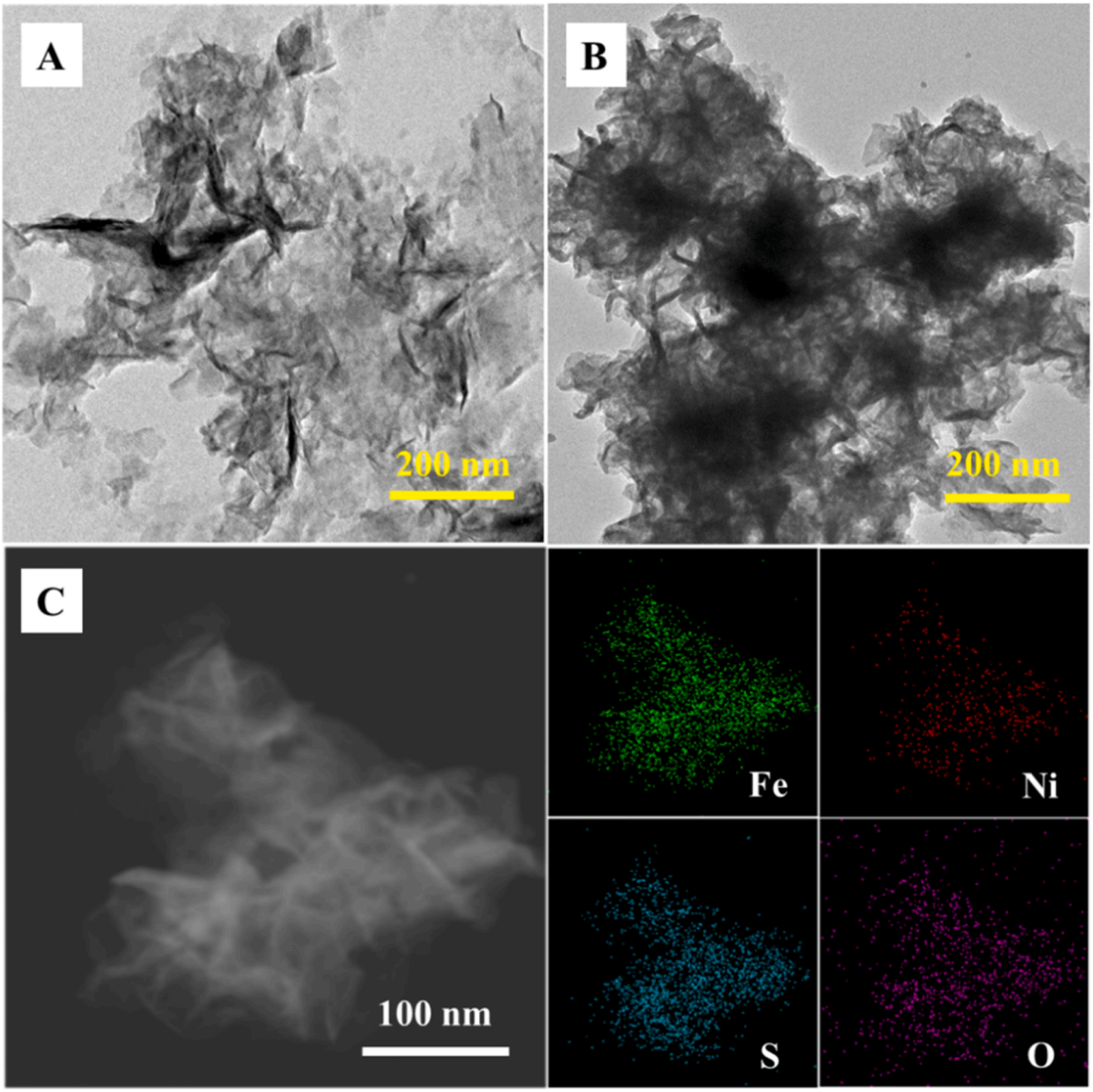

Fig. 9. (A) TEM image of the solid products in FeS system, (B) TEM image, and (C) TEM-EDS mapping of Fe, Ni, S, O elements in FeS/Ni^{2+} system. Experimental conditions: 1.0 g/L FeS, 10.0 mM BA, pH 7.0 reaction time of 0.5 h, and oxic conditions.

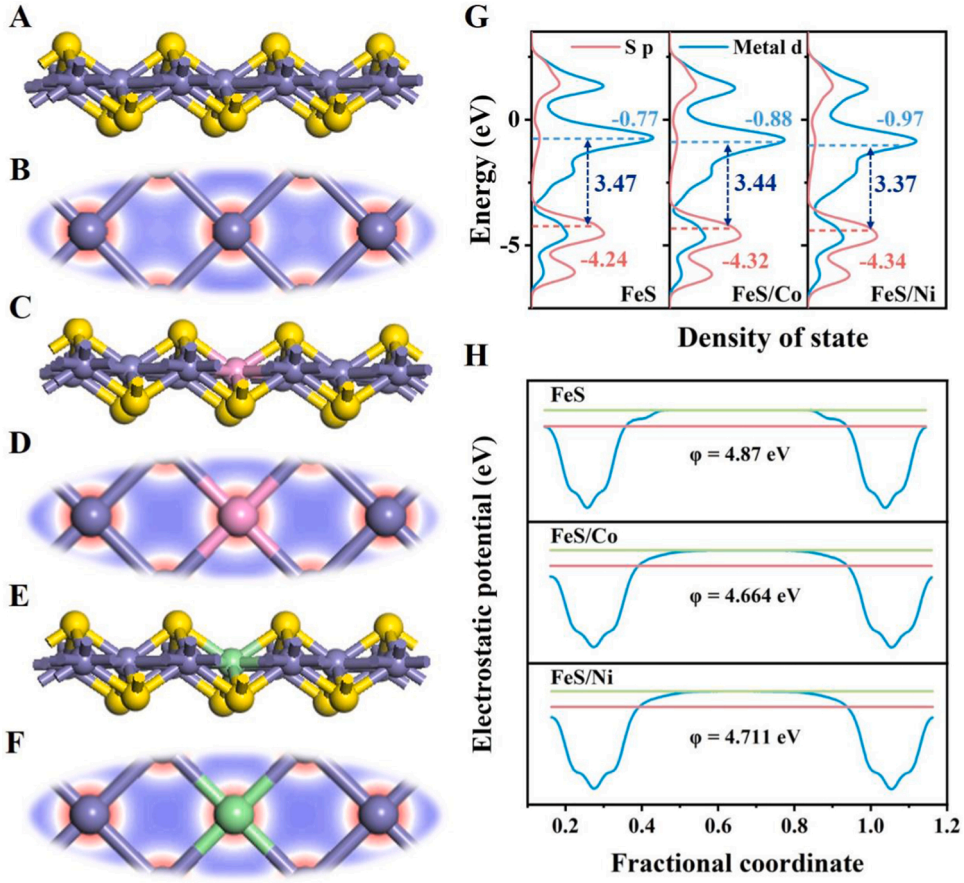

Fig. 10. (A-F) Optimized geometry and the electron density difference, (G) PDOS, and (H) work functions of FeS, FeS/Co, and FeS/Ni.

$$SO_3^{\bullet-} + O_2 \rightarrow SO_5^{\bullet-} \quad (10)$$

$$SO_3^{2-} + SO_5^{\bullet-} \rightarrow SO_4^{\bullet-} + SO_4^{2-} \quad (11)$$

3.4. Me^{2+} manipulated physicochemical properties of FeS

The physicochemical properties of FeS with the coexistence of Me^{2+} were systematically investigated to understand the mechanisms of accelerated Fe(III)/Fe(II) circulation as well as high-valence sulfur formation. Both TEM images and the elemental mappings showed that Fe, Ni, and S atoms were evenly dispersed in the FeS nanosheet (Fig. 9). The particles after aging in Me^{2+} solution for 5.0 h under anoxic conditions were characterized by using both XPS and FTIR measurements. It is shown that Ni and Co have both metallic and oxidized states (Fig. S23), attributed to the MeS and the relative metal oxides [54–56]. We also found MeS as well as the relative metal oxides in FeS/Me^{2+} systems at the reaction time of 0.5 h under oxic conditions (Fig. S24). Moreover, FTIR spectra showed that the stretching vibration of the Me-S shifted from 703 to 718 cm^{-1} with the presence of Me^{2+} (Fig. S25), further indicating the formation of Me-containing sulfides [57]. Furthermore, the oxidation products within the FeS reaction system after 1 h were characterized by DRFTIR spectra. As shown in Fig. 2C, the peak at 1643 cm^{-1} was assigned to the hydroxyl group bonded to the FeS surface, and another hydroxyl group located at 1620 cm^{-1} was assigned to lepidocrocite. It was found that the presence of Co and Ni caused the deviation of the two hydroxyl signals to 1681 and 1554 cm^{-1} respectively, suggesting the change of electronic structure of FeS after the addition of Me^{2+} [57,58], i.e., the formation of Me-containing sulfides.

The above results suggested that Me^{2+} adsorbed on the FeS surface could precipitate or replace Fe(II) in FeS, forming MeS or metal-substitute FeS, such as $Fe_{1-x}Me_xS$. Additionally, MeS itself could not activate O_2 to produce reactive oxidant (Fig. S26), and the direct addition of MeS into the FeS system only slightly promoted the degradation of BPA (Fig. S27). Therefore, it is reasonable to speculate that the promotion would be mainly attributed to the new phases of $Fe_{1-x}Me_xS$. Then, the electronic structure of FeS after the introduction of Me^{2+} was further investigated by density functional theory (DFT) calculations. After the lattice Fe was replaced by Co and Ni, electron rearrangement occurred (Fig. 10A-10 F). Further analysis revealed that the d band center was far from the Fermi level after the lattice Fe was replaced by Co and Ni (Fig. 10G), indicating that the active electronic states increased, thus facilitating electron transfer and improving electrical conductivity [59]. Moreover, the work function values followed the order of FeS/Co (4.664 eV) < FeS/Ni (4.711 eV) < FeS (4.870 eV) (Fig. 10H). The lower work function value of FeS/Co than FeS/Ni further indicated faster electron transfer in the FeS/Co^{2+} system, as lower work functions facilitate the escape of electrons from material surfaces [60].

Overall, the above results demonstrated that the introduction of Me^{2+} especially Co^{2+} resulted in the electronic regulation of FeS, thus facilitating Fe(II) regeneration through the electron transfer process from S^{2-} that converts into high-valence sulfur oxides.

4. Conclusions

This study demonstrated that the introduction of Co^{2+} and Ni^{2+} resulted in 3–10-fold improvements in the degradation of pollutant bisphenol A during FeS oxygenation. The enhanced degradation was attributed to the promoted generation of •OH and the facilitation of $SO_4^{\bullet-}$ production upon the addition of Co^{2+} and Ni^{2+}. Further investigations unveiled that these enhancements were a consequence of the accelerated circulation of Fe(III)/Fe(II) and the formation of high-valence

sulfur from S^{2-} when Co^{2+} or Ni^{2+} were present. Both experimental investigations and DFT calculations revealed that the introduction of Me^{2+} led to the formation of Me-containing sulfides, which altered the electronic structure of FeS, thus facilitating the electron transfer process during FeS oxygenation, consequently leading to accelerated Fe(III)/Fe(II) circulation as well as high-valence sulfur formation. These new findings highlight the positive role of Me^{2+} on FeS oxygenation, clarifying the geochemical cycling of Fe, S, and C and shedding light on the enhancement of contaminant remediation in aquifer environments.

CRediT authorship contribution statement

Rongrong Ding: Investigation, Methodology, Data curation, DFT calculation, Writing, Original draft. **Guannan Zhou:** Methodology, Data curation. **Chuanshu He:** Investigation, Reviewing and Editing. **Wenqiang Li:** Investigation. **Yiran Wang:** Investigation. **Xiaocheng Liu:** Methodology, Reviewing. **Bo Lai:** Reviewing and Editing. **Yang Mu:** Data curation, Writing, Reviewing and Editing, Supervision.

Declaration of Competing Interest

The authors declare that they have no known competing financial interests or personal relationships that could have appeared to influence the work reported in this paper.

Data availability

Data will be made available on request.

Acknowledgments

The authors wish to thank the National Natural Science Foundation of China (52025101, U19A20108, 51821006, 51878637, and 51908530) and the 2019 Annual Anhui Province Natural Science Foundation Youth Project of China (1908085QE210) for financially supporting this study and supercomputing center of USTC for computational support and infrared spectroscopy and microspectroscopy endstation (BL01B) in the National Synchrotron Radiation Laboratory (NSRL) in Hefei, China for DRFTIR analysis.

Appendix A. Supporting information

Supplementary data associated with this article can be found in the online version at doi:10.1016/j.apcatb.2023.123350.

References

[1] A.J. Pyzik, S.E. Sommer, Sedimentary iron monosulfides: Kinetics and mechanism of formation, Geochim. Cosmochim. Acta 45 (1981) 687–698.
[2] C. Zhou, Y. Zhou, B.E. Rittmann, Reductive precipitation of sulfate and soluble Fe (III) by Desulfovibrio vulgaris: Electron donor regulates intracellular electron flow and nano-FeS crystallization, Water Res 119 (2017) 91–101.
[3] E.C. Butler, K.F. Hayes, Effects of solution composition and ph on the reductive dechlorination of hexachloroethane by iron sulfide, Environ. Sci. Technol. 32 (1998) 1276–1284.
[4] P.J. Michael, V.N. Ronald, M.S. Jeno, Pyrrhotite reaction kinetics: reaction rates for oxidation by oxygen, ferric iron, and for nonoxidative dissolution, Geochim. Cosmochim. Acta 64 (2000) 1511–1522.
[5] J.L. Sun, J.R. Yang, Y.P. Liu, M.L. Guo, Q.Y. Wen, W.J. Sun, J.X. Yao, Y. Li, F. Jiang, Magnetically-mediated regeneration and reuse of core-shell Fe^0@Fe^{III} granules for in-situ hydrogen sulfide control in the river sediments, Water Res 157 (2019) 621–629.
[6] A. Ramesh Kumar, P. Riyazuddin, Seasonal variation of redox species and redox potentials in shallow groundwater: A comparison of measured and calculated redox potentials, J. Hydrol. 444–445 (2012) 187–198.
[7] D. Cheng, S.H. Yuan, P. Liao, P. Zhang, Oxidizing impact induced by mackinawite (FeS) nanoparticles at oxic conditions due to production of hydroxyl radicals, Environ. Sci. Technol. 50 (2016) 11646–11653.
[8] D. Cheng, A.K. Neumann, S.H. Yuan, W.J. Liao, A. Qian, Oxidative degradation of organic contaminants by FeS in the presence of O_2, Environ. Sci. Technol. 54 (2020) 4091–4101.
[9] W. Salomons, U.F.P. Mader, Heavy metals: problems and solutions, (1994).
[10] L.S. Miranda, B. Wijesiri, G.A. Ayoko, P. Egodawatta, A. Goonetilleke, Water-sediment interactions and mobility of heavy metals in aquatic environments, Water Res 202 (2021), 117386.
[11] N. Barlas, A pilot study of heavy metal concentration in various environments and fishes in the Upper Sakarya River Basin, Turkey, Environ. Toxicol. 14 (1999) 367–373.
[12] Z.L. He, X. Yang, P.J. Stoffella, Trace elements in agroecosystems and impacts on the environment, J. Trace Elem. Med. Biol. 19 (2005) 125–140.
[13] M. Sun, X.R. Ru, L.F. Zhai, In-situ fabrication of supported iron oxides from synthetic acid mine drainage: High catalytic activities and good stabilities towards electro-Fenton reaction, Appl. Catal. B-Environ. 165 (2015) 103–110.
[14] Mt Wolthers, S.J.V.D. Gaast, D. Rickard, The structure of disordered mackinawite, Am. Mineral. 88 (2003) 2007–2015.
[15] H.Y. Jeong, K.F. Hayes, Impact of transition metals on reductive dechlorination rate of hexachloroethane by mackinawite, Environ. Sci. Technol. 37 (2003) 4650–4655.
[16] J.W. Morse, T. Arakaki, Adsorption and coprecipitation of divalent metals with mackinawite (FeS), Geochim. Cosmochim. Acta 57 (1993) 3635–3640.
[17] Mishra, B., Encyclopedia of Materials: Science and Technology || Cobalt and Nickel Production, (2001) 1288–1294.
[18] S. Lehner, K.S. Savage, M. Ciobanu, D.E. Cliffel, The effect of As, Co, and Ni impurities on pyrite oxidation kinetics: an electrochemical study of synthetic pyrite, Geochim. Cosmochim. Acta 71 (2007) 2491–2509.
[19] H.Y. Jeong, K.F. Hayes, Reductive dechlorination of tetrachloroethylene and trichloroethylene by mackinawite (FeS) in the presence of metals: Reaction rates, Environ. Sci. Technol. 41 (2007) 6390–6396.
[20] E. Kim, J. Kim, Y. Chang, D. Turcioortega, P.G. Tratnyek, Effects of metal ions on the reactivity and corrosion electrochemistry of Fe/FeS nanoparticles, Environ. Sci. Technol. 48 (2014) 4002–4011.
[21] X.K. Tian, T.T. Luo, Y.L. Nie, J.B. Shi, Y.Y. Tian, D.D. Dionysiou, Y.X. Wang, New insight into a fenton-like reaction mechanism over sulfidated β-FeOOH: key role of sulfidation in efficient iron(III) reduction and sulfate radical generation, Environ. Sci. Technol. 56 (2022) 5542–5551.
[22] L. Chen, M. Tang, C. Chen, M.G. Chen, K. Luo, J. Xu, D. Zhou, F. Wu, Efficient bacterial inactivation by transition metal catalyzed auto-oxidation of sulfite, Environ. Sci. Technol. 51 (2017) 12663–12671.
[23] J. Xu, W. Ding, F. Wu, G. Mailhot, D. Zhou, K. Hanna, Rapid catalytic oxidation of arsenite to arsenate in an iron(III)/sulfite system under visible light, Appl. Catal. B Environ. 186 (2016) 56–61.
[24] Y.S. Zhang, H.B. Zhao, L. Qian, M.L. Sun, G.Z. Qiu, A brief overview on the dissolution mechanisms of sulfide minerals in acidic sulfate environments at low temperatures: Emphasis on electrochemical cyclic voltammetry analysis, Miner. Eng. 158 (2020), 106586.
[25] A. Schippers, W. Sand, Bacterial leaching of metal sulfides proceeds by two indirect mechanisms via thiosulfate or via polysulfides and sulfur, Appl. Environ. Microbiol. 65 (1999) 319.
[26] H.C. Alexander, D.C. Dill, L.W. Smith, P.D. Guiney, P. Dorn, Bisphenol a: Acute aquatic toxicity, Toxicol. Environ. Chem. 7 (1988) 19–26.
[27] M. Noszczynska, Z. Piotrowskaseget, Bisphenols: application, occurrence, safety, and biodegradation mediated by bacterial communities in wastewater treatment plants and rivers, Chemosphere 201 (2018) 214–223.
[28] L. Yan, Rapid Determination of Iron Sulfide Content in the Sludge of Bay and Lake by Electrochemical Methods (Doctor Thesis), Kochi-Tech. AC.,, 2006.
[29] T.C. Robinson, D.E. Latta, J. Leddy, M.M. Scherer, Redox potentials of magnetite suspensions under reducing conditions, Environ. Sci. Technol. 56 (2022) 17454–17461.
[30] H. Peng, C.I. Pearce, A.T. N'Diaye, Z.L. Zhu, J.R. Ni, K.M. Rosso, J. Liu, Redistribution of electron equivalents between magnetite and aqueous Fe^{2+} induced by a model quinone compound AQDS, Environ. Sci. Technol. 53 (2019) 1863–1873.
[31] Z.Z. Pan, B. Bártová, T. LaGrange, S.M. Butorin, N.C. Hyatt, M.C. Stennett, K. O. Kvashnina, R. Bernier-Latmani, Nanoscale mechanism of UO_2 formation through uranium reduction by magnetite, Nat. Commun. 11 (2020) 4001.
[32] L. Canesi, E. Fabbri, Environmental effects of BPA: focus on aquatic species, Dose Response 13 (2015), 1559325815598304.
[33] S. Flint, T. Markle, S. Thompson, E. Wallace, Bisphenol A exposure, effects, and policy: A wildlife perspective, J. Environ. Manag. 104 (2012) 19–34.
[34] M. Hussein, K. Yoneda, Z. Mohd-Zaki, A. Amir, N. Othman, Heavy metals in leachate, impacted soils and natural soils of different landfills in Malaysia: An alarming threat, Chemosphere 267 (2021), 128874.
[35] H.Q. Zhao, S.Q. Huang, W.Q. Xu, Y.R. Wang, Y.X. Wang, C.S. He, Y. Mu, Undiscovered mechanism for pyrogenic carbonaceous matter-mediated abiotic transformation of azo dyes by sulfide, Environ. Sci. Technol. 53 (2019) 4397–4405.
[36] T.X. Liu, X.M. Li, T.D. Waite, Depassivation of Aged Fe^0 by inorganic salts: implications to contaminant degradation in seawater, Environ. Sci. Technol. 47 (2013) 7350–7356.
[37] K. Parlinski, Z.Q. Li, Y. Kawazoe, FirSt-principles determination of the soft mode in cubic ZrO_2, Phys. Rev. Lett. 78 (1997) 4063–4066.
[38] G. Kresse, D. Joubert, From ultrasoft pseudopotentials to the projector augmented-wave method, Phys. Rev. B 59 (1999) 1758–1775.
[39] M. Ji, K. Umemoto, C.Z. Wang, K.M. Ho, R. Wentzcovitch, New ultrahigh pressure phases of H_2O ice predicted using an adaptive genetic algorithm, Phys. Rev. B. 84 (2011), 1894-1894.
[40] W. Liu, Z.H. Ai, M.H. Cao, L.Z. Zhang, Ferrous ions promoted aerobic simazine degradation with Fe@Fe_2O_3 core–shell nanowires, Appl. Catal. B Environ. 150–151 (2014) 1–11.

[41] M.J. Huang, Y. Han, W. Xiang, D.L. Zhong, C. Wang, T. Zhou, X.H. Wu, J. Mao, Situ-formed phenoxyl radical on the CuO surface triggers efficient persulfate activation for phenol degradation, Environ. Sci. Technol. 55 (2021) 15361–15370.
[42] N. Zrinyi, A.L. Pham, Oxidation of benzoic acid by heat-activated persulfate: Effect of temperature on transformation pathway and product distribution, Water Res 120 (2017) 43–51.
[43] X.L. Zhou, K. Mopper, Determination of photochemically produced hydroxyl radicals in seawater and freshwater, Mar. Chem. 30 (1990) 71–88.
[44] J. He, C.J. Miller, R.J. Collins, D.S. Wang, T.D. Waite, Production of a surface-localized oxidant during oxygenation of mackinawite (FeS), Environ. Sci. Technol. 54 (2020) 1167–1176.
[45] S.Q. Zhou, Y.H. Yu, Wq Zhang, X.Y. Meng, J.M. Luo, L. Deng, Z. Shi, J. Crittenden, Oxidation of microcystin-LR via activation of peroxymonosulfate using ascorbic acid: kinetic modeling and toxicity assessment, Environ. Sci. Technol. 52 (2018) 4305–4312.
[46] X.H. Long, Z.K. Xiong, R.F. Huang, Y.H. Yu, P. Zhou, H. Zhang, G. Yao, B. Lai, Sustainable Fe(III)/Fe(II) cycles triggered by co-catalyst of weak electrical current in Fe(III)/peroxymonosulfate system: collaboration of radical and non-radical mechanisms, Appl. Catal. B Environ. 317 (2022), 121716.
[47] H. Bataineh, O. Pestovsky, A. Bakac, pH-induced mechanistic changeover from hydroxyl radicals to iron(IV) in the Fenton reaction, Chem. Sci. 3 (2012) 1594–1599.
[48] P. Salgado, V. Melin, M. Albornoz, H. Mansilla, G. Vidal, D. Contreras, Effects of pH and substituted 1,2-dihydroxybenzenes on the reaction pathway of Fenton-like systems, Appl. Catal. B Environ. 226 (2018) 93–102.
[49] Y. Zhou, J. He, J. Lu, Y.D. Liu, Y.B. Zhou, Enhanced removal of bisphenol A by cyclodextrin in photocatalytic systems: Degradation intermediates and toxicity evaluation, Chin. Chem. Lett. 31 (2020) 2623–2626.
[50] K.J. Hou, Z.J. Pi, F. Chen, L. He, F.B. Yao, S.J. Chen, X.M. Li, H.R. Dong, Q. Yang, Sulfide enhances the Fe(II)/Fe(III) cycle in Fe(III)-peroxymonosulfate system for rapid removal of organic contaminants: Treatment efficiency, kinetics and mechanism, J. Hazard. Mater. 435 (2022), 128970.
[51] D.D. Boland, R.N. Collins, C.J. Miller, C.J. Glover, T.D. Waite, Effect of solution and solid-phase conditions on the Fe(II)-accelerated transformation of ferrihydrite to lepidocrocite and goethite, Environ. Sci. Technol. 48 (2014) 5477–5485.
[52] C. Brandt, R. Van Eldik, Transition metal-catalyzed oxidation of sulfur(IV) oxides. Atmospheric-relevant processes and mechanisms, Chem. Rev. 95 (1995) 119–190.
[53] Y.J. Choe, J.Y. Byun, S.H. Kim, J. Kim, Fe_3S_4/Fe_7S_8-promoted degradation of phenol via heterogeneous, catalytic H_2O_2 scission mediated by S-modified surface Fe^{2+} species, Appl. Catal. B-Environ. 233 (2018) 272–280.
[54] P.T. Wang, X. Zhang, J. Zhang, S. Wan, S.J. Guo, G. Lu, J.L. Yao, X.Q. Huang, Precise tuning in platinum-nickel/nickel sulfide interface nanowires for synergistic hydrogen evolution catalysis, Nat. Commun. 8 (2017) 14580.
[55] D.L. Legrand, H.W. Nesbitt, G.M. Bancroft, X-ray photoelectron spectroscopic study of a pristine millerite (NiS) surface and the effect of air and water oxidation, Am. Mineral. 83 (1998) 1256–1265.
[56] W.W. Xu, Z.Y. Lu, X.D. Lei, Y.P. Li, X.M. Sun, A hierarchical Ni–Co–O@Ni–Co–S nanoarray as an advanced oxygen evolution reaction electrode, Phys. Chem. Chem. Phys. 16 (2014) 20402–20405.
[57] X.E. Wang, F.F. Chen, G.A. Girard, H.J. Zhu, D.R. MacFarlane, D. Mecerreyes, M. Armand, P.C. Howlett, M. Forsyth, Poly(Ionic Liquid)s-in-salt electrolytes with co-coordination-assisted lithium-ion transport for safe batteries, Joule 3 (2019) 2687–2702.
[58] C. Feng, Z.R. Zhang, D.L. Wang, Y. Kong, J. Wei, R.Y. Wang, P.Y. Ma, H.L. Li, Z. G. Geng, M. Zuo, J. Bao, S.M. Zhou, J. Zeng, Tuning the electronic and steric interaction at the atomic interface for enhanced oxygen evolution, J. Am. Chem. Soc. (2022).
[59] J.B. Zhou, X.J. Liu, L.Q. Zhu, S.W. Niu, J.Y. Cai, X.S. Zheng, J. Ye, Y. Lin, L. Zheng, Z.X. Zhu, D. Sun, Z. Lu, Y.P. Zang, Y.S. Wu, J.X. Xiao, Q. Liu, Y.C. Zhu, G.M. Wang, Y.T. Qian, High-spin sulfur-mediated phosphorous activation enables safe and fast phosphorus anodes for sodium-ion batteries, Chem 6 (2020) 221–233.
[60] F. Chen, L.L. Liu, Y.J. Zhang, J.H. Wu, H.Q. Yu, Enhanced full solar spectrum photocatalysis by nitrogen-doped graphene quantum dots decorated BiO_{2-x} nanosheets: Ultrafast charge transfer and molecular oxygen activation, Appl. Catal. B Environ. 277 (2020), 119218.